Asian Journal of Chemistry; Vol. 35, No. 12 (2023), 3081-3086

ASIAN JOURNAL OF CHEMISTRY

https://doi.org/10.14233/ajchem.2023.30681

Impact of (Sm, Sr) Co-Doping at Bi-Site on the Structural, Optical, Multiferroic and Dielectric Properties of Bismuth Ferrite Nanocomposites

SHAHNAZ KOSSAR

School of Natural Sciences, GNA University, Sri Hargobindgarh, Phagwara-Hoshiarpur Road, Phagwara-144401, India

Corresponding author: E-mail: shazia.rajput0505@gmail.com; shahnaz.kossar@gnauniversity.edu.in

Received: 6 October 2023; *Accepted*: 10 November 2023; *Published online*: 2 December 2023; AJC-21472

A series of samarium (Sm) and strontium (Sr) co-doped $BiFeO_3$ (BFO) and pure $BiFeO_3$ (BFO) nanocomposites were synthesized by the sol-gel auto-combustion method. The X-ray diffraction pattern of the synthesized Sr:Sm BFO nanocomposites shows a rhombohedral perovskite structure. The morphological studies revealed that synthesized Sr:Sm BFO and pure BFO exhibit a regular arrangement of grains. The diffuse reflectance spectra (DRS) exhibit the doping of Sr:Sm BFO reduces the optical band gap values of BFO from 2.02 eV to 1.69 eV. It was observed that the prepared Sr:Sm BFO and undoped BFO samples show G-type antiferromagnetic behaviour and the values of saturation magnetization (M_s) increased by increasing the Sr:Sm BFO doping concentrations at the A site of BFO lattice. The magnitude of the dielectric constant (ε_r) and dielectric loss (tan δ) were increased gradually with applied frequency and by increasing doping concentration in the BFO matrix. The significant enhancement in the dielectric parameters with increasing Sm and Sr concentrations in BFO results in improved ferromagnetic properties that could be considered a promising candidate for some advanced device applications.

Keywords: Bismuth ferrite, Samarium, Strontium, Co-doping, Bismuth Ferrites, Dielectric, Ferromagnetic.

INTRODUCTION

Multiferroic materials are unique and show both ferroelectric and (anti)ferromagnetic properties at room temperature simultaneously [1]. With the coexistence of such interesting properties, bismuth ferrite ($BiFeO_3$, BFO) leads to the exciting and potential applications in the field of electronic devices, such as data storage [2], spintronics [3], sensors [4] and in ultrasonic devices [5]. The availability of multiferroic materials in nature is extremely limited due to the competition between the ferromagnetic and ferroelectric orders [6]. Among the various solid-state multiferroic materials, bismuth ferrite (BFO) is one of the conventional single-phase multiferroic materials, which shows saturated magnetization at room temperature and limits the applicability of these materials [7]. BFO has the highest ferroelectric Curie temperature (Tc ~ 1123 K) and the highest antiferromagnetism Neel temperature (TN ~ 647 K). Moreover, BFO has a rhombohedral distorted and perovskite structure with the space group *R*3*c*. Due to the coupling between ferroelectric and ferromagnetic properties, BFO has a potential and a promising candidate to explore the possibilities to improve its properties to make it suitable for applications in memory devices, spintronics and sensors [8]. In BFO, the ferroelectric feature was attributed to Bi^{3+} ions having lone pair electrons and Fe^{3+} ions, which have partially filled inner shells, were attributed to the ferromagnetic behaviours [9]. However, the large leakage current in BFO due to the presence of secondary phases and oxygen vacancies (VO) defects is usually a significant drawback restricting possible applications. Several kinds of studies have been carried out in efforts to improve the properties of $BiFeO_3$, such as doping with different alkaline and alkaline-earth ions elements [10], the post-annealing process by suppressing the valence fluctuations of Fe ions and results in separaation of oxygen vacancies and by improving the electronic, ferromagnetic properties in BFO [11]. Among the several processes, doping of rare earth and transition materials at A and B (A: Bi, B: Fe) sites is the best choice to improve the leakage current, which helps to improve the ferromagnetic properties in BFO matrix [12]. The doping of trivalent rare earth ions, including Gd^{3+} [12], La^{3+} [13], Sm^{3+} [14], Ho^{3+} [15], *etc.* or divalent alkaline metal ions such as Ba^{2+} [16], Ca^{2+} [16], Sr^{2+} [11], *etc*. at the A-site of BFO can enhance the ferromagnetic properties

by replacing a part of ions in BFO lattice [11]. Among all the various dopants, samarium and strontium be the promising one because which has ionic radii of Sm^{3+} (1.061 Å) and Sr (1.261 Å), which is closer to that of Bi^{3+} (1.03 Å) that could stabilize oxygen octahedron ions and helps to suppress the Bi^{3+} vacancies and tends to improve the ferroic properties [16]. Hence, co-doping of Sr:SmBFO is expected to enhance the ferromagnetic behaviours in the BFO matrix significantly. Recent researchers have shown that co-doping of rare earth (RE) and transition metal (TM) ions into BFO host materials improves ferromagnetic characteristics [12-16]. Priya *et al.* [10] studied the La/Cu: BFO nanocomposites prepared by a sol-gel method at room temperature showing enhanced ferromagnetic properties [10]. Jangra *et al.* [17] studied the Cr:Co and Mn co-doped multiferroic BFO nanocomposites, which show the improved dielectric and magnetic properties compared to pure BFO.

The present research aims is to synthesize the Sr:Sm BFO nanocomposites by sol-gel auto-combustion method and investigated the structural, ferromagnetic and dielectric behaviours. The doping of Sm and Sr at A-site of BFO is varied as $Sm_{0.7}Bi_{0.93}Sr_xFeO_3$ with $x = 0.0$ (Sr(0):Sm BFO), 0.02 (Sr(2):Sm BFO), 0.05(Sr(5):Sm BFO), 0.07(Sr(7):SmBFO) and 1.0 (Sr(10): Sm BFO). The structural studies were examined using X-ray diffraction and surface morphology by FESEM techniques. The ferromagnetic and dielectric properties of Sr:SmBFO samples were also investigated at room temperature.

EXPERIMENTAL

Iron(III) nitrate nonahydrate ($Fe(NO_3)_3·9H_2O$), Sigma, 99%), strontium nitrate $Sr(NO_3)_2$, Sigma, 99%), bismuth nitrate pentahydrate ($Bi(NO_3)_3·5H_2O$, Sigma, 99%), samarium nitrate hexahydrate ($Sm(NO_3)_3·6H_2O$, Sigma, 99%) and citric acid ($C_6H_8O_7$, LOBA Chemie, purity ≥ 99.5%) were used as precursors. For the preparation of solvents, distilled water and dilute nitric acid (HNO_3) were used.

For the preparation of pure bismuth ferrite and samarium, strontium co-doped bismuth ferrite nanocomposites. Initially, 0.015 M of $Bi(NO_3)_3·5H_2O$ was added successively into 15 mL of de-ionized distilled water and dil. HNO_3 and kept on stirring continuously for 30 min. Equal molarity of $Fe(NO_3)_3·9H_2O$ was dissolved into di-ionized distilled water and stirred for 30 min at room temperature. For the preparation of Sm and Sr co-doped $BiFeO_3$, the doping concentrations of Sm was fixed as 7 wt.% and Sr concentration were varied as 2 wt.%, 5 wt.%, 7 wt.% and 10 wt.%, respectively. A sufficient amount of $Sm(NO_3)_3·6H_2O$ and $Sr(NO_3)_2$ were added dropwise to the base solution of $Bi(NO_3)_3·5H_2O$ and $Fe(NO_3)_3·9H_2O$. The chelating agent, citric acid with 0.015 M were dissolved in deionized distilled water individually and then mixed together with constant magnetic stirring under ambient temperature. Therefore, the obtained brown transparent-gel was formed due to evaporation of water and was subjected to heat at 90 ºC under constant stirring for 3 h. Finally, the obtained gel was converted into powder by autocombustion process and the precipitates were grinded and annealed at 450 ºC for 4 h. By using the hydraulic pellet press, the pellets were prepared from the annealed powders with 7 mm thickness under six tons pressure. For the electrical measurements, silver paste was applied on both sides of the pellets. The synthesized nanocomposites for pure BFO and Sm, Sr co-doped BFO (2 wt.%, 5 wt.%, 7 wt.% and 10 wt.%) were coded as pure BFO, Sr(2):SmBFO, Sr(5): SmBFO, Sr(7):SmBFO and Sr(10):SmBFO, respectively.

The phase identification of undoped BFO and Sr:SmBFO nanocomposites was examined by X-ray diffraction technique [(XRD, Bruker D8 Diffractometer (Cu$K\alpha$, $\lambda = 1.5406$ Å)). A field emission scanning electron microscope (FESEM) was used to investigate the surface morphology (FEI Quanta 200 F). The UV-Vis spectroscopy was used to determine the optical characteristics (Shimadzu, UV 3600 PLUS). The magnetization hysteresis (M–H) loops of undoped BFO and Sr:SmBFO nanocomposites were measured at room temperature using vibrating sample magnetometer (Lake Shore). The dielectric studies were carried out using LCR meter (SOLARTRON, SI-1260).

RESULTS AND DISCUSSION

Structural studies: Fig. 1a illustrates the structural analysis of the synthesized Sr(2):SmBFO, Sr(5):SmBFO, Sr(7):SmBFO and Sr(10):SmBFO nanocomposites. Both undoped BFO and co-doped (Sr:SmBFO) nanocomposites confirms the formation of rhombohedral perovskite structure with the space group *R*3*c*. All the peaks were exactly matched with JCPDS card no. 86-1518 [12]. The obtained XRD peaks were correlated with reflections from (012), (104), (110), (006), (202), (024), (116), (018) and (214) planes, respectively. Upon addition of samarium and strontium, the impurity phases were observed at about 28º, which were related to $Bi_2Fe_4O_9$ and Bi_2O_3. The observed secondary phases was associated due to its kinetics formation and metastable nature [17]. As the co-doped of Sr, Sm is added into the A-site of BFO site, the intensity of the (104) and (110) planes increases and showing a higest maximum for SS(7): BFO, which indicates that the crystallinity of BFO matrix has improved. Moreover, for higher doping concentration at SS (10 at.%) in the BFO matrix which leads to degrade the crystalline characteristics, possibily due to an increase in micro-strain of the BFO lattice [18]. In addition, the impurity phases gradually decreases upon increasing the concentrations of Sm and Sr into BFO matrix, which may be associated to an increase in micro-strain of the BFO [19]. The average crystallite sizes D (nm) of the synthesize BFO nanocomposites were determined using the Scherrer's formula [12].

$$D = \frac{k\lambda}{\beta\cos\theta} \quad (1)$$

where D is the crystalline size of the most intense peak, k is Scherrer's constant, λ is the wavelength of the incident radiations (1.54 Å), β denotes the full-width at half maxima (FWHM) in radians of the most intense peak and θ denotes the Bragg's angle diffraction. The average crystallite size of pure BFO is about 31 nm and Sr(2):SmBFO, Sr(5):SmBFO, Sr(7):SmBFO and Sr(10):SmBFO nanocomposites were found to be 32, 34, 37 and 29 nm, respectively. Therefore, it is observed that the crystallite size of the codoped samples increases when BFO is doped with Sm and Sr ions.

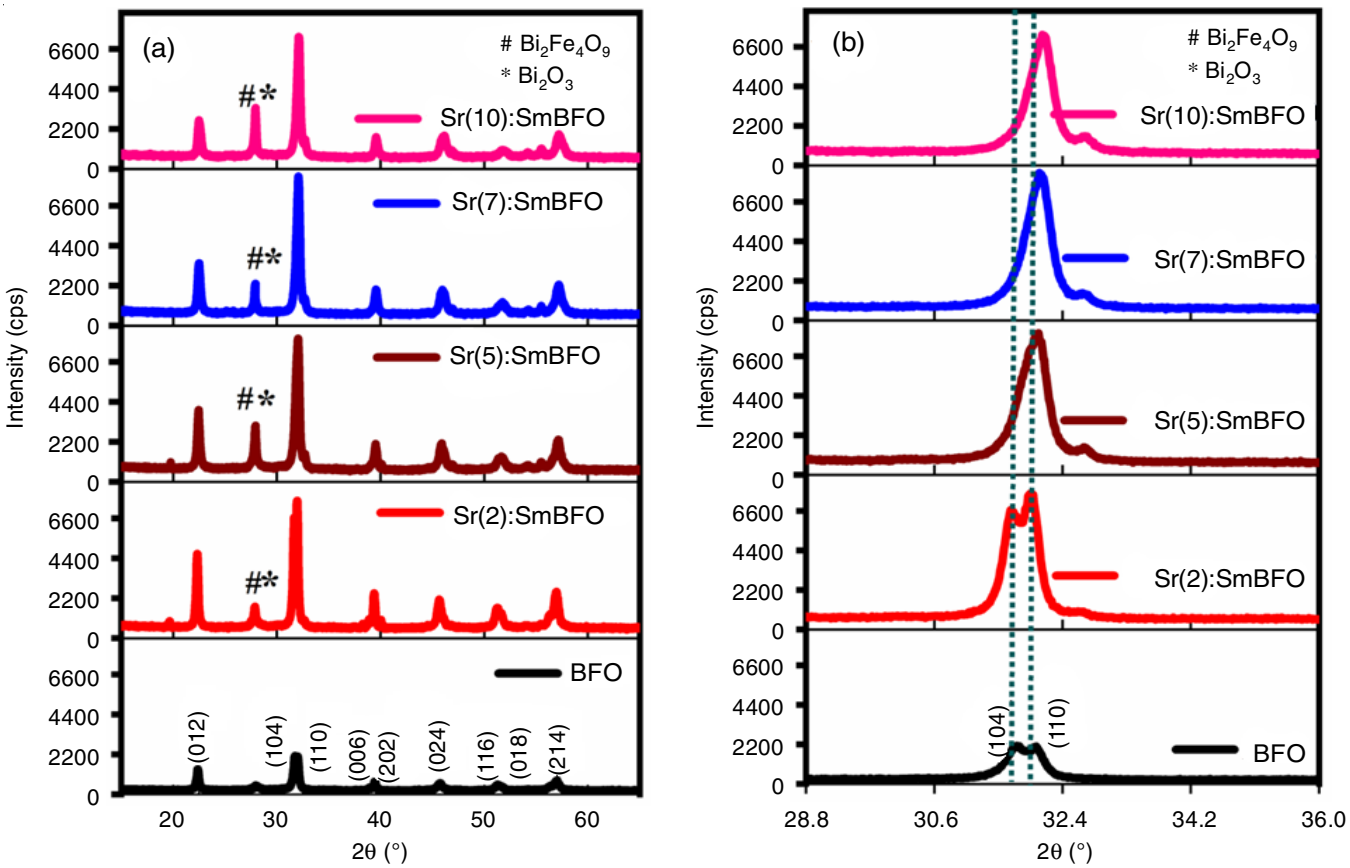

Fig. 1. (a) Structural analysis and (b) enlarged view in the peaks of (104) and (110) for the synthesized pure BFO, Sr(2):SmBFO, Sr(5):SmBFO, Sr(7):SmBFO and Sr(10):SmBFO nanoparticles

Fig. 1b shows the enlarged view in the peaks of (104) and (110) pure BFO, Sr(2):SmBFO, Sr(5):SmBFO, Sr(7):SmBFO and Sr(10):SmBFO nanocomposites. The structrual studies revealed that with higher Sr(7):SmBFO doping concentrations in BFO, the two prominent diffractions planes of (104) and (110) are merged into single peak, resulting into the structural distortion from rhombohedral to tetragonal phase in the BFO lattice [19]. Such structural modification by adding codoping of Sr: SmBFO nanocomposites could pave the way towards improved ferromagnetic properties in BFO matrix [20]. Furthermore, the merging of the peaks at higher doping indicates that the dopants have been incorporated at the BFO lattice, which confirm is the lattice distortion.

Morphological analysis: Fig. 2 shows the FESEM images of pure BFO, Sr(2):SmBFO, Sr(5):SmBFO, Sr(7):SmBFO and Sr(10):SmBFO nanocomposites. It was revealed that from the analysis, the shape of the surface morphology appears to be non-uniform and irregular.

Optical studies: Fig. 3a depicts the UV-visible absorption spectrum for pure BFO, Sr(2):SmBFO, Sr(5):SmBFO, Sr(7): SmBFO and Sr(10):SmBFO nanocomposites. The spectra were determined from the diffuse reflectance (R) spectrum by using the Kulbeka-Munk function [$(F(R) = (1 - R)^2/2R)$]. From the analysis of absorption spectrum, it was revealed that the bands lies in the different regions such as UV region around 233 nm, charge transfer (C–T) band around 362 nm, which is associated

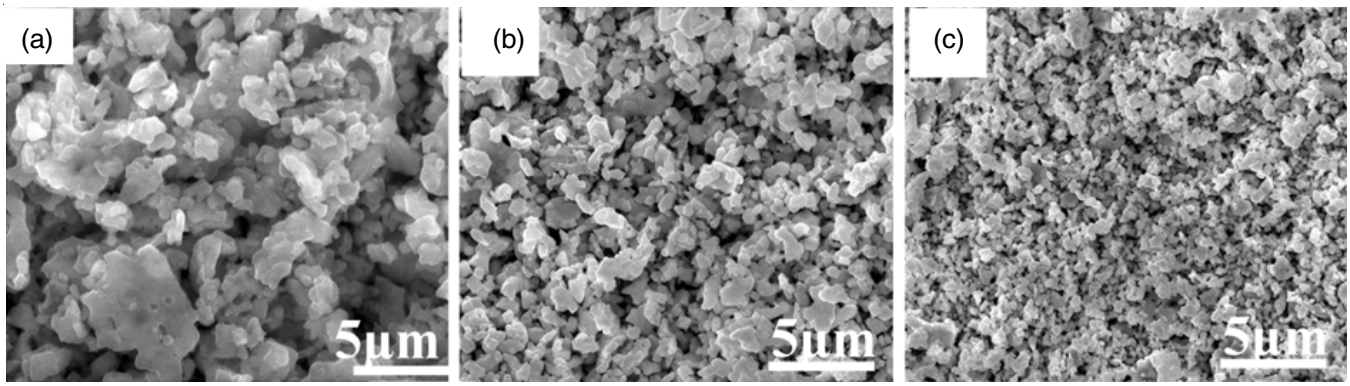

Fig. 2. FESEM micrograph of pure BFO, Sr(2):SmBFO, Sr(7):SmBFO and Sr(10):SmBFO nanocomposites

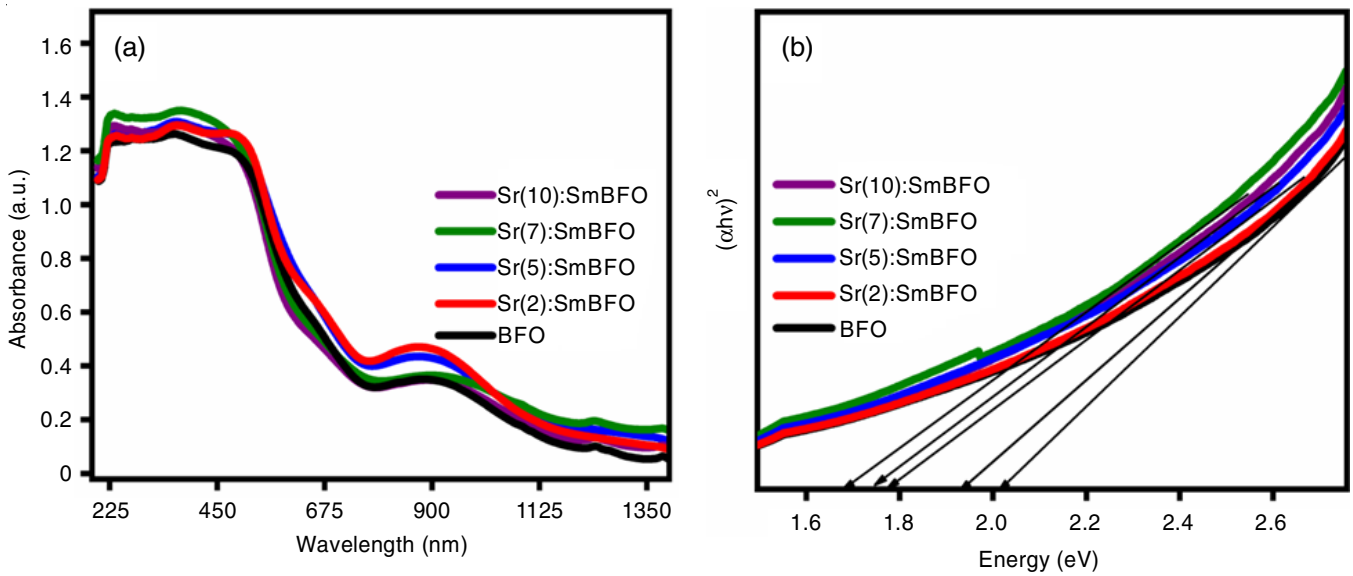

Fig. 3. (a) Ultra violet-visible absorption spectrum and (b) optical band gap for pure BFO, Sr(2):SmBFO, Sr(5):SmBFO, Sr(7):SmBFO and Sr(10):SmBFO nanoparticles

with transitions from bismuth-oxygen (Bi–O). In the visible region, the band of 517 nm corresponds to the C–T band from the Fe–O states. The transition around 665 nm and 897 nm correspond to double degenerated *d–d* transitions of Fe^{3+}. The shifts around 665 nm and 897 nm usually associated with a double *d–d* transition of Fe^{3+} ions [21]. From the absorption spectrum, the energy band gap (E_g) was determined using the following Tauc's equations [12]:

$$Ah\nu = A\,(h\nu - E_g)^n \quad (1)$$

where α is the absorption coefficient, E_g is the optical energy, 'A' is the constant, hν is the absorption energy and n is 1/2 represents the direct band gap semiconductors. The Kulbeka-Munk function was used for calculating band gap energies by extrapolating photon energy (hν) *versus* $(ah\nu)^2$ for pure BFO, Sr(2):SmBFO, Sr(5):SmBFO, Sr(7):SmBFO and Sr(10):SmBFO nanocomposites. When Sm,Sr doping concentration is increased in the BFO matrix, then the optical band gap (E_g) values will decreases from 2.02 eV to 1.69 eV (Fig. 3b). Generally, there are several approaches to reduce the optical band energy (E_g) of single-doped and co-doped BFO nanocomposites, such as chemical binding, microstructure deformation, oxygen vacancy (V_O) defects and reduction in particle size [11]. According to the first-principles calculations, the diminished degree of hybridizations was developed by the stable combination of Sm^{3+} and Sr^{2+} ions, which tends to reduce the gap between the valence band and conduction band of pure BFO nanocomposites [11]. Moreover, the changes in Fe-O–Fe and Fe-O bond lengths induced by the Sr:SmBFO nanocomposites will significantly affect one-electron bandwidth (W) and hence decrease in band gap values [11,12]. According to the empirical formulation, there is a direct relationship between the bond length angle, bond length, the optical band gap, $W \propto \frac{\cos\omega}{d_{Fe-O}^{3.5}}$, where d_{Fe-O} is the bond-length of Fe–O and ω is ½[π–(Fe–O–Fe)]. The optical energy band gap is analogous with W and mentioned as E_g = Δ–W, where Δ represents the energy charge–transfer [11,12].

Magnetic properties: Fig. 4 shows the magnetic hysteresis (M-H) loops for pure BFO, Sr(2):SmBFO, Sr(5):SmBFO, Sr(7):SmBFO and Sr(10):SmBFO for the synthesized nanocomposites. All samples were recorded under ambient temperature with external applied field of 1500 kOe. Table-2 shows the ferromagnetic parameters of remnant magnetization (M_r) and saturation magnetization (M_s), which were calculated from M-H hystresis loops. It was observed that the pure BFO sample shows weak ferromagnetism, which can be further, improved by adding of co-doping of Sm and Sr into the BFO samples. Generally, the undoped BFO sample shows the weak ferromagnetic order due to the spin cycloidal, which shows G-type antiferromagnetic characterstics with saturation magnetization (M_s) of 0.041 emu/g. The obtained weak ferromagnetic characteristics may be explained by a magnetic cycloid has a long period of wavelength (λ = 62 nm), which restrictis the macroscopic magnetization and ferromagnetic interactions between Fe^{2+}–O–Fe^{3+} in BFO matrix [12]. Upon co-doping of Sm and Sr at A-site of BFO, the saturation magnetization (M_s) significantly improved. For Sr(2):SmBFO, Sr(5):SmBFO, Sr(7):SmBFO and Sr(10):SmBFO nanocomposites, the value of M_s were calculated as 0.047, 0.053, 0.11 and 0.070 emu/g, respectively. The enhanced value of saturation magnetization (M_s) in co-doped BFO samples could be attributed to various strategies such as (i) when Sm^{3+} ions were added, the space modulated spin structure collapses resulting in a long range antiferromagnetic order [22]; (ii) addition of Sr atoms at A or B-site may occurs an octahedral tilt and change the bond angle between Fe-O-Fe and Fe-O [23]. However, Sr(10):SmBFO shows the minimum value of Ms (0.053 emu/g), which is due to the maximum suppression of impurity phases, leakage current and the difference in ionic radii of Sm^{3+} (0.958 Å), Sr^{2+} (1.12 Å) and Bi^{3+} (1.03 Å) ions which may alter the spiral modulated spin structure of BFO as a result, causing an enhanced in the magnetization in BFO lattice. Therefore,

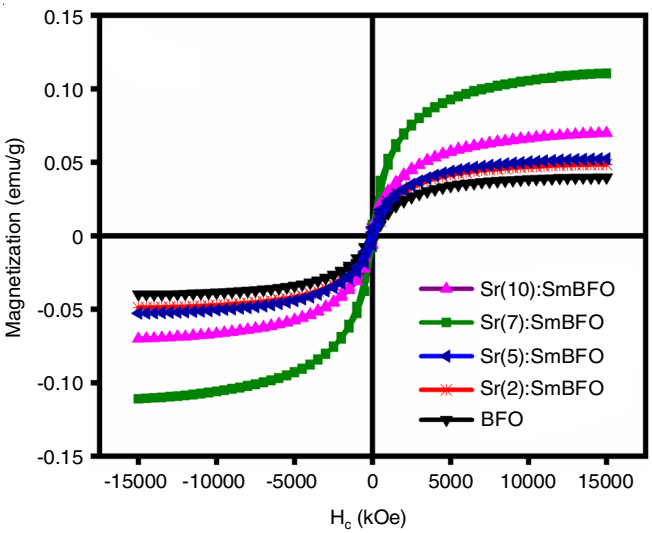

Fig. 4. Magnetic hysteresis (M-H) loops for pure BFO, Sr(2):SmBFO, Sr(5):SmBFO, Sr(7):SmBFO and Sr(10):SmBFO nanoparticles for the synthesized nanocomposites

such an enhancent the ferromagnetic properties of co-doped BFO may further improve the dielectric properties in BFO matrix [11,12].

Dielectric analysis: Fig. 5a-b show the dielectric loss (tan δ) and dielectric constant (ε_r') of pure BFO, Sr(2):SmBFO, Sr(5):SmBFO, Sr(7):SmBFO and Sr(10):SmBFO of the synthesized nanocomposites. All the samples were carried out at room temperature as a function of frequency in the range from 1 kHz and 1 MHz. In the high-frequency range, the dielectric constant values observed in BFO were governed by ionic and electronic polarization, whereas the dielectric loss (tan δ) was influenced by the movement of domain walls in BFO at lower frequency range [24]. It was observed that from Fig. 5a, with the increase of applied frequencies, dielectric constant (ε_r') and dielectric loss (tan δ) gradually decreases and it remains constant nearly at high frequencies [11,12]. The decrease in the real component can be attributed to the relaxation of the dielectric. The observed behaviour of Sr:SmBFO nanocomposites can be attributed to the space charge relaxation effect, which can explained by Koop's phenomenological theory and Maxwell-Wagner (MW) model [25]. At lower frequency, the electrons between Fe^{2+} and Fe^{3+} ions were situated at the grain boundaries through the hopping-process which ocuurs large polarization and results in a high dielectric constant value of BFO nanocomposites. At a higher frequency region, most of the electrons would reverse directions with respect to applied field and less number of chance to enter into the grain boundaries region of BFO, which results to decrease the saturation magnetization (M_s) with a low dielectric constant value of BFO [12,24].

The dielectric constant of co-doped Sr:SmBFO increases significantly with increasing doping concentrations. In undoped BFO, the oxygen vacancy defects and displacement of Fe^{3+} ions and secondary phases leads to relatively high conductivity and less dielectric constant. Such reduction in leakage current helps to supress the oxygen vacancies (V_o) defect in undoped BFO, which further improving the dielectric properties [23]. Such improvement in the dielectric properties of co-doped Sr:SmBFO nanocomposites may be explained on the basis of ionic radii difference between Bi^{3+} (1.03 Å), Sm^{3+} (0.94 Å) and Sr^{2+} (1.12 Å). When Sm and Sr ions were added at the A-site of Bi^{3+} ions, it results in the reduction of the BFO crystal lattice and may lead to the variation of Fe–O bond. As a result, the dielectric properties of the co-doped BFOs were enhanced significantly, resulting in an increase in the magnetic properties as well [11]. In present research work, it was observed the same trend in the co-doped BFO samples in BFO matrix. As the concentration of Sr and Sm co-doped BFO was increased from Sr(2):SmBFO to Sr(10):SmBFO nanocomposites, the magnetic saturation, dielectric characteristics improved significantly. For high frequency applications, the Sr(7):SmBFO nanocomposites exhibit high dielectric constants and saturation values, they may be an excellent choice for high frequency applications.

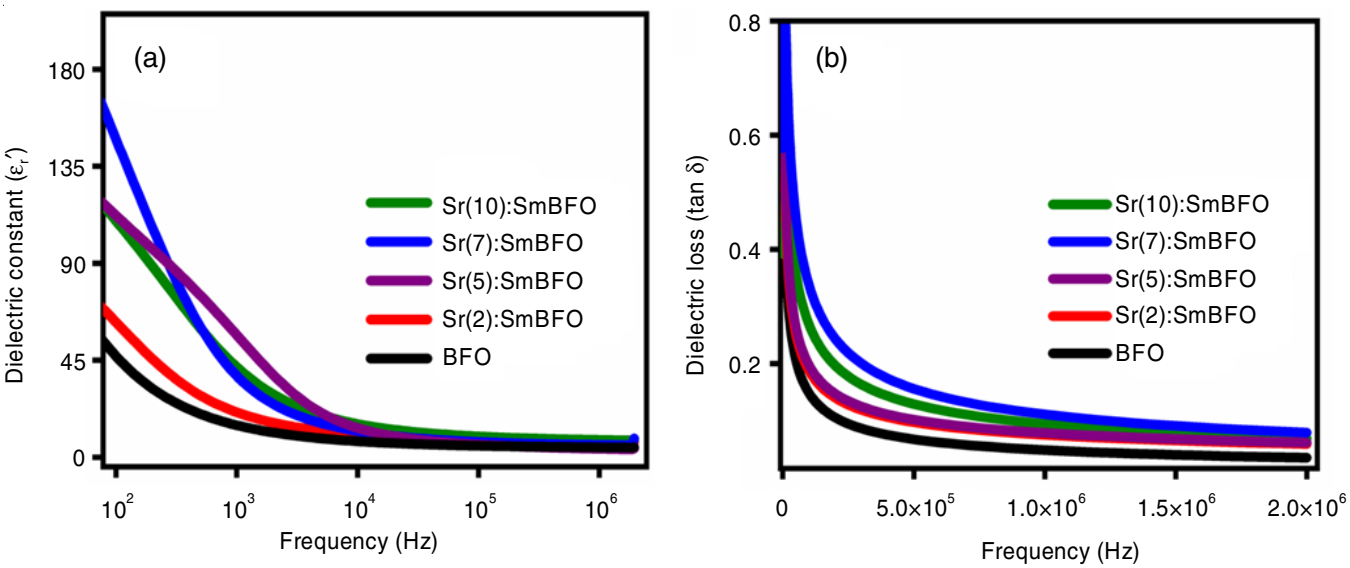

Fig. 5. (a) Dielectric constant (ε_r') and (b) dielectric loss (tan δ) of pure BFO, Sr(2):SmBFO, Sr(5):SmBFO, Sr(7):SmBFO and Sr(10):SmBFO nanoparticles

Conclusion

The present research work focused on Sr:SmBFO and pure BFO were synthesized by the sol–gel autocombustion method. The structrual, surface morphological, dielectric parameters and ferromagnetic properties of the prepared BFO and Sr:SmBFO samples were investigated. It is found that the doping concentration of Sr:SmBFO has a strong influenced on the material properties. The increase of Sr:SmBFO content leads to simultaneous increases the intensity of crystalline structure, tunability in energy band gap, magnetic saturation and dielectric parameters. The significant enhancement in the dielectric parameters with increasing samarium and strontium concentrations in BFO, which results in increases ferromagnetic properties that could be considered as a promising candidate for some of the advance device applications. The Sr(7):SmBFO nanocomposites shows the highest dielectric loss (tan δ) and significant enhancement in magnetic saturation, which is the best choice for tunable device applications.

ACKNOWLEDGEMENTS

The author acknowledge the award of GNA University seed money (Ref No: GU/RESEARCH/2022-23/036).

CONFLICT OF INTEREST

The authors declare that there is no conflict of interests regarding the publication of this article.

REFERENCES

1. A. Bismibanu, M. Alagar, I.B.S. Banu, P.R. Vanga, T. Selvalakshmi and M. Ashok, *Braz. J. Phys.*, **52**, 1 (2022); https://doi.org/10.1007/s13538-021-01004-4
2. N. Wang, X. Luo, L. Han, Z. Zhang, R. Zhang, H. Olin and Y. Yang, *Nano-Micro Lett.*, **12**, 81 (2020); https://doi.org/10.1007/s40820-020-00420-6
3. D. Sando, A. Agbelele, D. Rahmedov, J. Liu, P. Rovillain, C. Toulouse, I.C. Infante, A.P. Pyatakov, E. Jacquet, C. Carrétéro, C. Deranlot, S. Fusil, S. Lisenkov, D. Wang, J.-M. Le Breton, M. Cazayous, A. Sacuto, J. Juraszek, A.K. Zvezdin, L. Bellaiche, B. Dkhil, A. Barthélémy and M. Bibes, *Nat. Mater.*, **12**, 641 (2013); https://doi.org/10.1038/nmat3629
4. S. Kossar, R. Amiruddin and A. Rasool, *Micro Nano Syst. Lett.*, **9**, 1 (2021); https://doi.org/10.1186/s40486-020-00128-7
5. Y. Chen, K. Mei, C.-M. Wong, D. Lin, H. Chan and J. Dai, *Actuators*, **4**, 127 (2015); https://doi.org/10.3390/act4020127
6. B. Behera, B.C. Sutar and N.R. Pradhan, *Emergent Mater.*, **4**, 847 (2021); https://doi.org/10.1007/s42247-021-00223-4
7. A.S. Priya, D. Geetha and I.B. Shameem Banu, *Braz. J. Phys.*, **51**, 1438 (2021); https://doi.org/10.1007/s13538-021-00961-0
8. A.T.S. Sudandararaj, G.S. Kumar, M. Dhivya, R.D. Eithiraj and I.B.S. Banu, *J. Alloys Compd.*, **783**, 393 (2019); https://doi.org/10.1016/j.jallcom.2018.11.205
9. S.D. Lakshmi and I.B.S. Banu, *J. Sol-Gel Sci. Technol.*, **89**, 713 (2019); https://doi.org/10.1007/s10971-018-4901-x
10. A.S. Priya, I.B.S. Banu and M. Chavali, *Arab. J. Sci. Eng.*, **40**, 2079 (2015); https://doi.org/10.1007/s13369-015-1668-z
11. M.M. Rhaman, M.A. Matin, M.A. Hakim and M.F. Islam, *Mater. Sci. Eng. B*, **263**, 114842 (2021); https://doi.org/10.1016/j.mseb.2020.114842
12. S. Kossar, I.B. Shameem Banu, N. Aman and R. Amiruddin, *J. Dispers. Sci. Technol.*, **42**, 2053 (2021); https://doi.org/10.1080/01932691.2020.1806861
13. R.C. Oliveira, E.A. Volnistem, E.A.C. Astrath, G.S. Dias, I.A. Santos, D. Garcia and J.A. Eiras, *Ceram. Int.*, **47**, 20407 (2021); https://doi.org/10.1016/j.ceramint.2021.04.049
14. Y. Gu, Y. Zhou, W. Zhang, C. Guo, X. Zhang, J. Zhao, Y. Zhang and H. Zheng, *AIP Adv.*, **11**, 045223 (2021); https://doi.org/10.1063/5.0042485
15. Y. Wang, Y. Wang, M. Wei, J. Zhang and Y. Zhang, *J. Supercond. Nov. Magn.*, **32**, 3495 (2019); https://doi.org/10.1007/s10948-019-5108-2
16. C. Yang, C.Z. Liu, C.M. Wang, W.G. Zhang and J.S. Jiang, *J. Magn. Magn. Mater.*, **324**, 1483 (2012); https://doi.org/10.1016/j.jmmm.2011.11.033
17. S. Jangra, S. Sanghi, A. Agarwal, M. Rangi, K. Kaswan and S. Khasa, *J. Alloys Compd.*, **722**, 606 (2017); https://doi.org/10.1016/j.jallcom.2017.06.132
18. N.A. Taisan, S. Kumar and A. Alshoaibi, *Crystals*, **12**, 1610 (2022); https://doi.org/10.3390/cryst12111610
19. I.B. Shameem Banu and S.D. Lakshmi, *J. Mater. Sci. Mater. Electron.*, **28**, 16044 (2017); https://doi.org/10.1007/s10854-017-7504-3
20. Z.J. Li, Z.-L. Hou, W.-L. Song, X.-D. Liu, D.-W. Wang, J. Tang and X.-H. Shao, *Mater. Lett.*, **175**, 207 (2016); https://doi.org/10.1016/j.matlet.2016.04.016
21. N. Sharma, S. Kumar, A.K. Mall, R. Gupta and A. Garg, *Mater. Res. Express*, **4**, 015702 (2017); https://doi.org/10.1088/2053-1591/aa5579
22. G.S. Arya, R.K. Sharma and N.S. Negi, *Mater. Lett.*, **93**, 341 (2013); https://doi.org/10.1016/j.matlet.2012.11.131
23. I.B. Shameem Banu, S.D. Lakshmi, S. Kossar and N. A. Ahrar Mundari, Substitution Driven Optical and Magnetic Properties of Neodymium and Nickel Doped $BiFeO_3$ Ceramics for Spintronics Applications, 2018 International Conference on Recent Trends in Electrical, Control and Communication (RTECC), Malaysia, Malaysia, pp. 93-98 (2018); https://doi.org/10.1109/RTECC.2018.8625635
24. J. Khajonrit, U. Wongpratat, P. Kidkhunthod, S. Pinitsoontorn and S. Maensiri, *J. Magn. Magn. Mater.*, **449**, 423 (2018); https://doi.org/10.1016/j.jmmm.2017.10.092
25. S.C. Mazumdar, S. Datta and F. Alam, *Z. Angew. Math. Phys.*, **10**, 2026 (2022); https://doi.org/10.4236/jamp.2022.106138